Quantum sensing of time-dependent magnetic signals with molecular spins

Matteo Lanza,[1,2,*] Claudio Bonizzoni,[1,2] Olga Mironova,[3] Fabio Santanni,[4] Alessio Nicolini,[3] Alberto Ghirri,[2] Andrea Cornia,[3] and Marco Affronte[1,2]

[1] *Dipartimento di Scienze Fisiche, Informatiche e Matematiche, Università degli Studi di Modena e Reggio Emilia, via G. Campi 213/A, 41125 Modena, Italy*

[2] *Istituto Nanoscienze CNR, Centro S3, via G. Campi 213/A, 41125 Modena, Italy*

[3] *Dipartimento di Scienze Chimiche e Geologiche e UdR INSTM, Università degli Studi di Modena e Reggio Emilia, via G. Campi 103, 41125 Modena, Italy*

[4] *Dipartimento di Chimica "U. Schiff", Università di Firenze, Via della Lastruccia 3, Sesto F.no 50019, Italy*

(Received 17 September 2025; revised 8 January 2026; accepted 4 February 2026; published 13 March 2026)

Molecular spins offer a promising platform for quantum sensing, particularly in organic, supramolecular, and biological environments. Recognition of signals by these systems is of particular interest given their possible integration into more complex structures and their possible use as sensors in close proximity to analytes. In this work, we develop two quantum sensing protocols that enable discrimination between different time-dependent magnetic fields without requiring their periodicity to match the microwave manipulating sequence. These are based on the Hahn echo sequence and have been tested on VO(TPP) and $VOPt(SOCPh)_4$ molecular spins embedded in a superconducting yttrium barium copper oxide (YBCO) microwave planar resonator. We report a magnetic field sensitivity up to $2.57 \times 10^{-7}\ \mathrm{T\,Hz^{-\frac{1}{2}}}$ (with lower bounds approaching $2.87 \times 10^{-8}\ \mathrm{T\,Hz^{-\frac{1}{2}}}$) for signals with a duration of a few microseconds. Under the given conditions, the minimum signal area that can be measured is in the 10^{-10} T s range, suggesting a potential trade-off between the minimum measurable field, and the required signal duration and the memory time.

DOI: 10.1103/56hv-qp5d

I. INTRODUCTION

Quantum sensing exploits the quantum properties of a system to detect a physical quantity. Nuclear and electron spin systems with sufficiently long coherence times have the potential to be used for this purpose [1]. Nitrogen-vacancy (NV) centers in diamond are prototypical examples, having shown remarkable performance [2–5], including single-spin detection through optically detected magnetic resonance (ODMR) [4,6] and microwave (MW) dynamical decoupling schemes [4,6–10]. A large collection of NV centers acts as an average of the single-spin responses [4] and provides sufficiently large luminescent signals. This allows typical sensitivities of the order of $10^{-9}\ \mathrm{T\,Hz^{-\frac{1}{2}}}$ to be reached when detecting ac magnetic fields whose period is matched to the free precession time of protocols within dynamical decoupling sequences [7,9,10], and down to $10^{-12}\ \mathrm{T\,Hz^{-\frac{1}{2}}}$ with the use of a continuous heterodyne detection scheme [11].

Molecular spins, besides their microsecond coherence times [12], greatly benefit from chemical design, a powerful way to control their composition and their local environment, tune their energy levels and incorporate them into supramolecular structures or crystalline 3D or 2D lattices [13–15]. Their portability, i.e., the possibility of the sensor being attached to an analyte with atomic precision at nanometer distance, is one of their most interesting features. In fact, molecular-spin labels have already been used to measure distances within a single protein, in combination with pulsed electron-electron double resonance (PELDOR) sequences [16]. In this respect, they constitute a valuable resource for spin-based quantum sensing [17–19], and the development of sensing protocols can expand their potential in this field [20–26]. We have shown the possibility of using molecular spins as quantum memories [27] and, more recently, for quantum sensing of ac magnetic fields [26]. Along this line, the detection of a nonperiodic time-dependent magnetic field signal would allow the recognition of specific events; however, due to the higher number of harmonics expected and the fact that the microwave protocols cannot match their period, this is

*Contact author: matteo.lanza@unimore.it

a more complex task. For instance, this has been demonstrated in state-of-the-art experiments on NV centers in diamond through ODMR protocols [28–31]. Nonetheless, the sequences used in these works employ optical initialization and detection [32], several MW pulses [31], multiple triggering of the external signal [29], or a combination of these elements.

In this work, we propose two spin echo sequences that consist of only two MW pulses and do not require optical readout. For both protocols, based on a Hahn echo sequence [33], the microwave pulses or the external signal are moved to allow for the discrimination of different signal shapes. In contrast to more conventional ac magnetometry protocols, the external signal does not need to have a period that matches the total sequence time. Furthermore, the external magnetic signal needs to be triggered only once per sequence repetition, and it does not need a specific time alignment with the MW sequence (i.e., it does not have to be entirely contained between the two MW pulses at the beginning of the protocol). The sensing principle relies on the difference in the phase accumulation obtained during the two free-precession times of the sequence at successive steps. We perform our tests on molecular spins at liquid-helium temperature using planar superconducting MW resonators; however, we note that our protocols can also be implemented at room temperature and in a commercial spin-resonance spectrometer, with potential application to a variety of spin systems.

II. EXPERIMENTAL DETAILS

A. Setup

A high-T_C yttrium barium copper oxide (YBCO) superconducting coplanar resonator is used for the manipulation and readout of the spin system with MW pulse sequences. The resonator has a bandwidth BW_r of a few megahertz (2–10 MHz) throughout the experiments. This value can be tuned at room temperature by changing the distance between the MW feed antenna and the resonator. Possible effects related to the resonator bandwidth are considered in Sec. IV and in the Supplemental Material [34]. The sample is placed at the center of the resonator, where the generated MW magnetic field, $B_{1,MW}$,

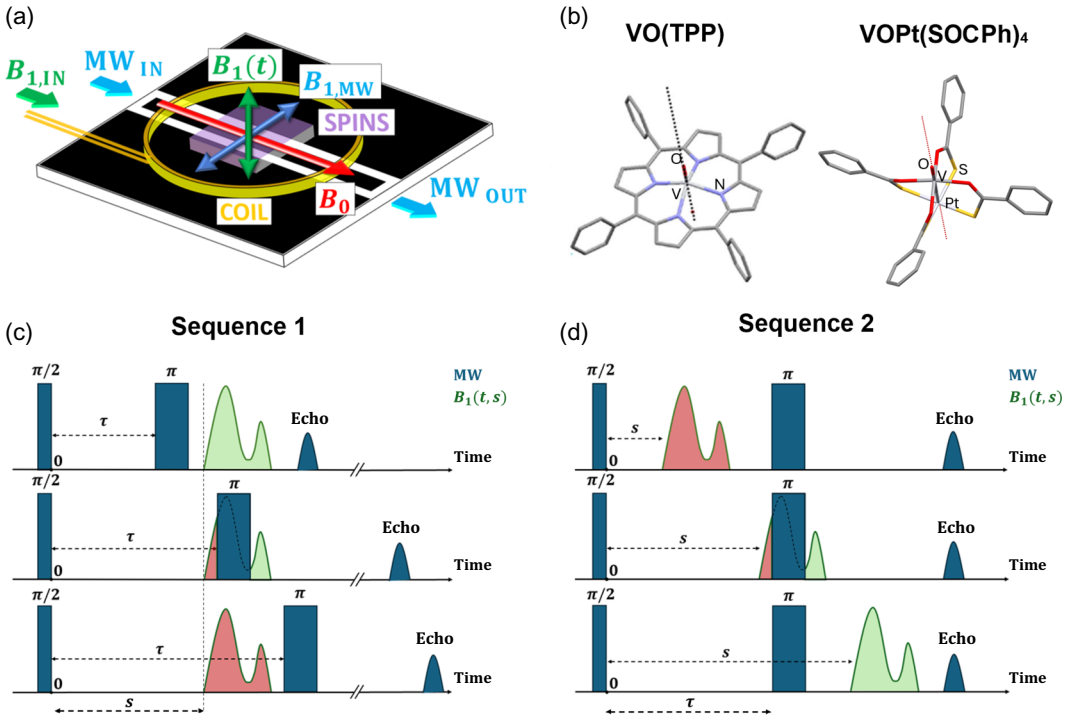

FIG. 1. (a) YBCO superconducting coplanar resonator used to deliver the MW pulses, $B_{1,MW}$. The sample is placed in the middle of the resonator, and it is surrounded by an rf copper coil used to deliver the external magnetic field to be measured, $B_1(t)$. The static field, B_0, is applied along the longitudinal axis of the resonator. Figure reproduced from Ref. [26] under CC license. (b) Molecular structures of VO(TPP) (left) and $VOPt(SOCPh)_4$ (right). The picture of the VO(TPP) molecule is adapted from Ref. [27] under CC license. (c) Sequence 1: the two MW pulses (blue) are used to generate an echo, and the interpulse delay τ is changed step by step while the position of the magnetic field signal, s, is held fixed. (d) Sequence 2: the interpulse delay is kept fixed while the position of the magnetic field signal is swept across the whole sequence by increasing s step by step. In both (c),(d), the phase accumulation is proportional to the difference between the signal areas remaining before and after the π pulse (opposite phase precession signs are represented with red and green shaded areas).

has its maximum, as shown in Fig. 1(a). In addition, a copper coil is placed on top of the resonator, surrounding the sample, to generate a calibrated magnetic signal, $B_1(t)$. A static magnetic field, B_0, is applied along the longitudinal axis of the resonator. In this configuration, all three fields (B_0, $B_{1,\mathrm{MW}}$, and $B_1(t)$ are perpendicular to each other; Fig. 1) [26]. The MW pulses are generated using a homemade heterodyne setup in which a mixer modulates a gigahertz frequency ($\nu_0 - \nu_{\mathrm{IF}}$) with a lower $\nu_{\mathrm{IF}} = 70$ MHz frequency carrying the desired pulse pattern [27]. The readout of the system is performed through a spin echo, which can be detected in both phase and amplitude using a second mixer receiving $\nu_0 - \nu_{\mathrm{IF}}$ as a reference frequency. Both ν_{IF} and the signal for the coil are generated using two different channels of an arbitrary-waveform generator (AWG) [26]. A quantum design physical property measurement system (QD-PPMS) is used for cooling the sample to 2–3.5 K and applying the static magnetic field in the plane of the YBCO resonator.

B. Sequences

The Hahn echo sequence consists of two MW pulses: an initial $\pi/2$ pulse induces a 90° spin rotation on the Bloch sphere; this is followed by a free-precession time, τ, and finally by a π pulse that causes a refocusing [33]. When an external magnetic field $B_1(t)$ is applied using the coil, the echo undergoes a phase accumulation [1]:

$$\phi_{\mathrm{echo}}(T_{\mathrm{seq}}, s) = \int_0^{T_{\mathrm{seq}}} \gamma B_1(t, s) dt, \tag{1}$$

where T_{seq} is the time between the $\pi/2$ pulse and the spin echo (total sequence time), and γ is the transduction parameter (with units deg/T s). Here, we introduce a dependence on s, which is a rigid time shift of $B_1(t)$ with respect to the end of the $\pi/2$ pulse; this is used to move the signal across the MW sequence. Equation (1) can be split into three different intervals for the phase accumulation: between the $\pi/2$ pulse and the π pulse, during the application of the π pulse, and between the π pulse and

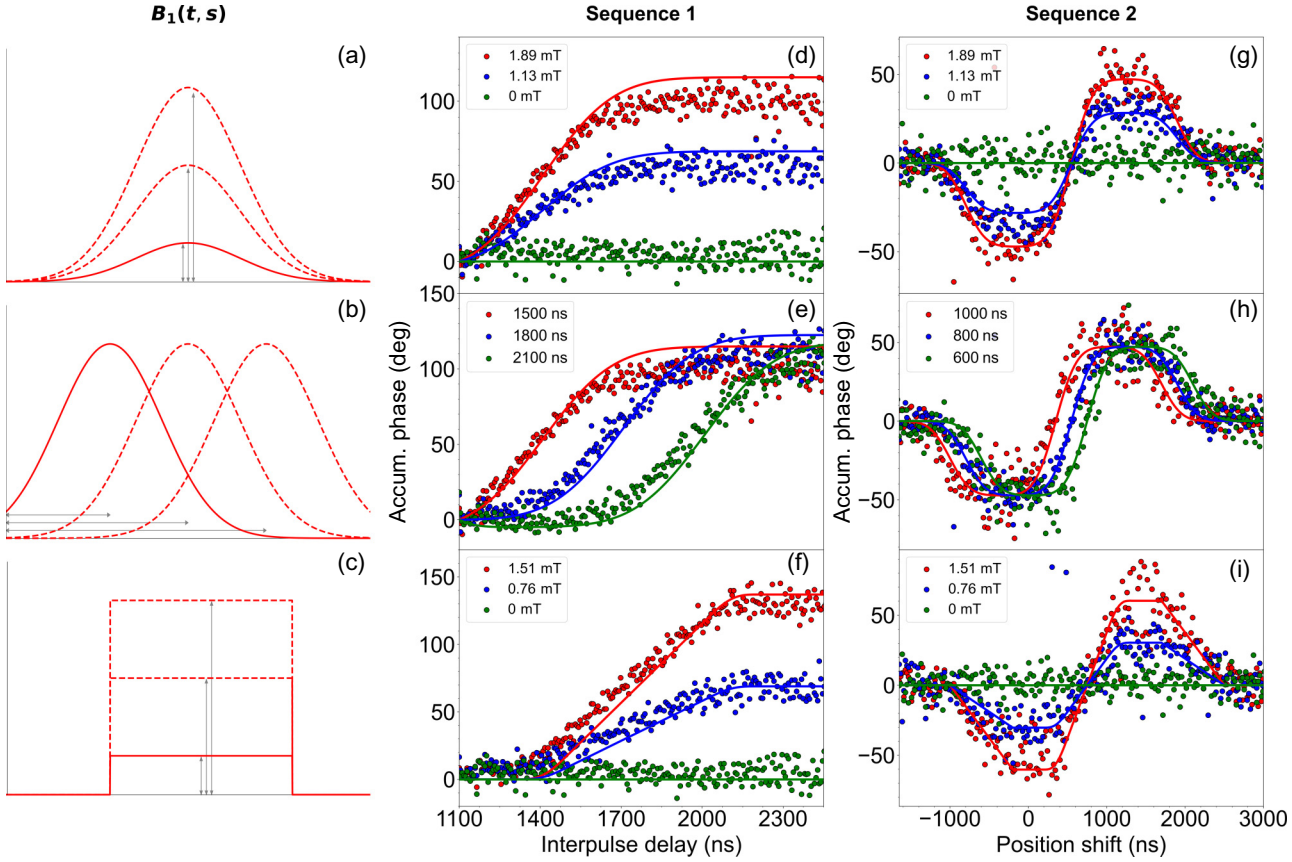

FIG. 2. Sequences 1 and 2 performed on VO(TPP) at 2–3.5 K and at a fixed value of the static field B_0. The protocols are tested with (a),(b) a Gaussian signal or with (c) a rectangular signal. (d),(g) Phase accumulation measured for different amplitudes, $B_{1,\mathrm{max}}$, of the Gaussian signal for (d) Sequence 1 and (g) Sequence 2. (e),(h) Phase accumulation measured when the central position, t_0, of the Gaussian signal is changed in both (e) Sequence 1 and (h) Sequence 2. (f),(i) The amplitude, $B_{1,\mathrm{max}}$, of the rectangular signal is changed in both (f) Sequence 1 and (i) Sequence 2. For Sequence 1, an experimental baseline has been removed (see Supplemental Material for details [34]). In all panels, experimental data are shown with dots, while solid lines represent calculated curves obtained with Eq. (2).

the spin echo [Figs. 1(c) and 1(d)]. In the third region, the accumulated phase has an opposite sign with respect to the first one due to the refocusing introduced by the π pulse. In the second region, the phase accumulation is modulated by a sine function due to the rotation of the magnetization on the Bloch sphere [29]. The expression for the phase accumulation is

$$\begin{aligned}\phi_{\text{echo}}(T_{\text{seq}}, s) &= \int_{t_{\frac{\pi}{2},\text{end}}}^{t_{\pi,\text{start}}} \gamma B_1(t,s)dt \\ &- \int_{t_{\pi,\text{start}}}^{t_{\pi,\text{end}}} \gamma B_1(t,s) \sin\left(\frac{t - t_{\pi,\text{start}} - \frac{T_\pi}{2}}{T_\pi/\pi}\right) dt \\ &- \int_{t_{\pi,\text{end}}}^{t_{\text{echo}}} \gamma B_1(t,s)dt, \end{aligned} \tag{2}$$

where $t_{\frac{\pi}{2},\text{end}}$ is the time at which the $\pi/2$ pulse ends, $t_{\pi,\text{start}}$ and $t_{\pi,\text{end}}$ are the start and end times for the π pulse, respectively. T_π is the duration of the π pulse, and t_{echo} is the time at which the echo is observed. Hereafter, we will fix $t_{\frac{\pi}{2},\text{end}} = 0$ ns.

Since the phase accumulated during a Hahn echo sequence depends on the area of the external signal through Eq. (2), it is possible to exploit the opposite signs obtained in the different regions to detect an external nonperiodic signal. This can be achieved with two different sequences: Sequence 1 [Fig. 1(c)] consists of a Hahn echo sequence in which the interpulse delay (τ) is increased step by step, shifting the π pulse over the external signal $B_1(t,s)$, which remains unchanged in its starting position by fixing s. For each step, an echo is recorded, and its phase depends on the area of the signal according to Eq. (2). The total duration of the sequence is related to the interpulse delay through the relation $T_{\text{seq}} = 2\tau + T_\pi$. Conversely, in Sequence 2 [see Fig. 1(d)], the $\pi/2$ and π pulses have fixed τ, and the external signal is shifted rigidly step by step in time by increasing s, while the MW sequence remains unchanged. The accumulated phase appearing in Eq. (2) now depends on the position shift, s, while T_{seq} remains unchanged.

In both Sequence 1 and Sequence 2, the key features of the time-dependent $B_1(t,s)$ signal can be derived from the behavior of the phase of the echo signal through Eq. (2).

C. Molecular-spin samples

Both samples contain vanadyl complexes ($S = \frac{1}{2}$, $I = \frac{7}{2}$) magnetically diluted in a diamagnetic matrix of their isostructural titanyl analogues. The first sample is a solid solution of VO(TPP) (2 mol %) in TiO(TPP), used as a powder with an estimated $T_{\text{m}} \approx 2$ μs (at 2 K) and a spin density $\rho = 2.3 \times 10^{19}$ spin/cm^3 [15,35]. The second sample is a solid solution of VOPt(SOCPh)$_4$ [36,37] (1 mol %) in TiOPt(SOCPh)$_4\cdot$ 2THF, used as a single crystal with an estimated $T_{\text{m}} \approx 4$ μs (at 3 K) and $\rho = 1.0 \times 10^{19}$ spin/cm^3 [38]. The two samples give similar electron paramagnetic resonance (EPR) spectra, and the strongest transition line is chosen by fixing the static-field value to match the energy of the YBCO resonator. Further information on the sample preparation, orientation, and memory-time estimation can be found in the Supplemental Material [34].

III. RESULTS

We first test our sequences by applying a Gaussian magnetic field signal of the form

$$B_1(t,s) = B_{1,\text{max}} e^{\left(-\frac{(t-(t_0+s))^2}{2\sigma^2}\right)}, \tag{3}$$

where $B_{1,\text{max}} = B_1(t_0 + s)$ is the amplitude of the external field at the center of the Gaussian, $t_0 + s$ is its central position in time, and σ is its width. Here, the aim is to distinguish the effects of changing one parameter ($B_{1,\text{max}}$, t_0, σ) at a time while the others are kept fixed.

As a further test, we use a rectangular external signal with the equation

$$B_1(t,s) = \begin{cases} 0, & \text{if } t < t_{\text{L}} + s, \\ B_{1,\text{max}}, & \text{if } t_{\text{L}} + s \le t \le t_{\text{R}} + s, \\ 0, & \text{if } t > t_{\text{R}} + s, \end{cases} \tag{4}$$

where $B_{1,\text{max}}$ is the amplitude of the signal and $t_{\text{L}} + s$ and $t_{\text{R}} + s$ are the left- and right-hand time extremes with respect to the time origin, respectively.

A. Quantum sensing with VO(TPP)

A powder sample of magnetically diluted VO(TPP) is used to initially assess the efficiency of the two protocols. Sequences 1 and 2 are repeated with a Gaussian signal [Eq. (3)] for different values of $B_{1,\text{max}}$ and t_0 [Figs. 2(a), 2(d), and 2(g) and Figs. 2(b), 2(e), and 2(h), respectively]. This allows us to evaluate whether the protocols are capable of sensing changes in the amplitude and position of the external signal. The resulting echo phase signals [Figs. 2(d) and 2(e)] show clear differences in both the amount of accumulated phase and the starting position of the accumulation with respect to the timescale. We also test the protocols with a rectangular signal [Eq. (4)] by varying its amplitude [Figs. 2(c), 2(f), and 2(i)]. The phase accumulation clearly depends on the value of $B_{1,\text{max}}$.

B. Quantum sensing with VOPt(SOCPh)$_4$

To investigate the effect of the memory time, T_{m}, we use a single crystal of magnetically diluted VOPt(SOCPh)$_4$. Experiments are carried out at a fixed static field by applying Gaussian and rectangular signals. The resulting phase

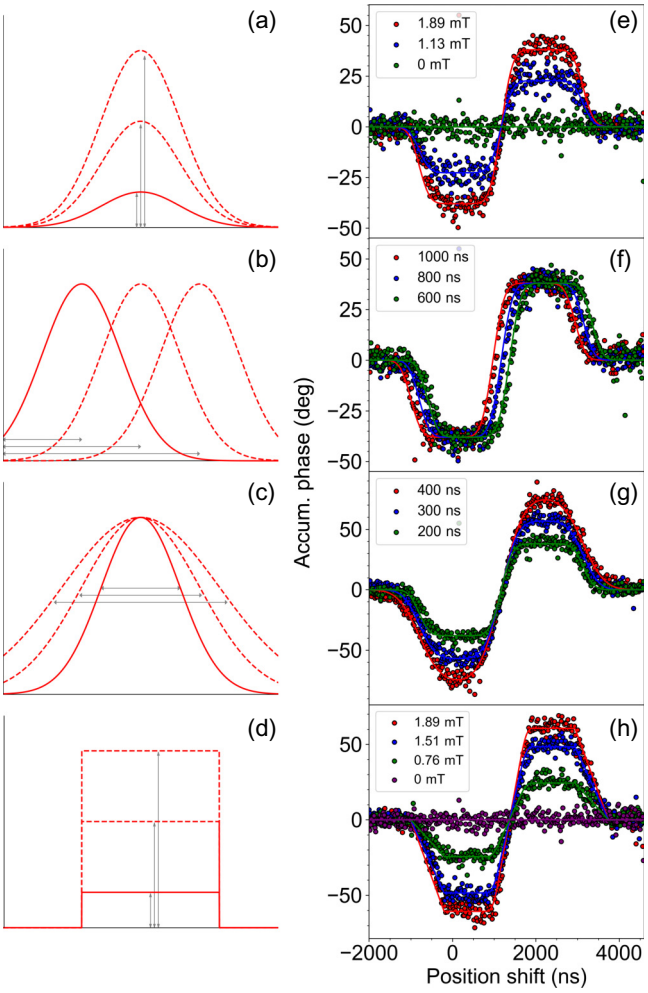

FIG. 3. Tests performed with Sequence 2 on $VOPt(SOCPh)_4$ at ≈3 K and at a fixed static field (B_0). (a)–(c) Gaussian and (d) rectangular signals are used. (e)–(g) Phase accumulation measured when (e) the amplitude $B_{1,max}$, (f) the central position t_0, and (g) the width σ of the Gaussian signal are progressively increased. (h) Phase of the echo measured for different amplitudes $B_{1,max}$ of a rectangular pulse signal. In all panels, the dotted traces represent experimental points, while the solid lines represent calculated curves obtained according to Eq. (2)).

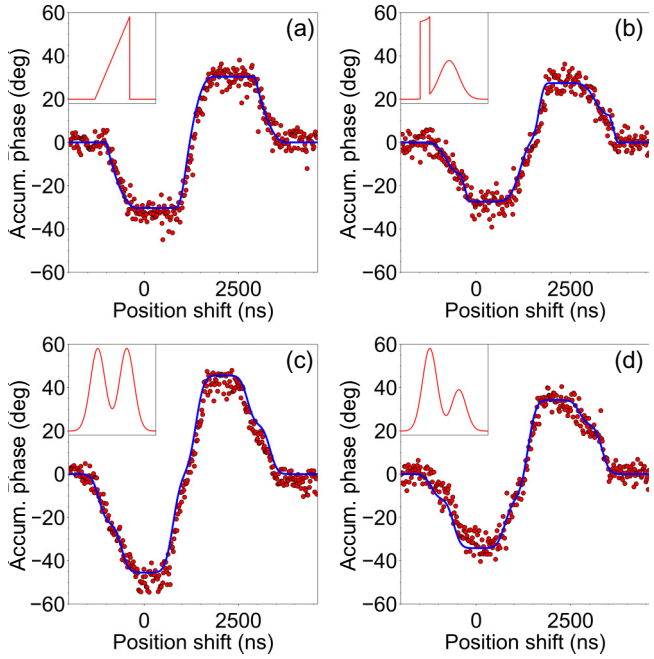

FIG. 4. Phase accumulation of the echo obtained with Sequence 2 on $VOPt(SOCPh)_4$ for differently shaped external signals (sketched in inset): (a) sawtooth, (b) rectangular wave + Gaussian, (c) double Gaussian, and (d) asymmetric double Gaussian. The experimental data are shown as red dots. The solid blue lines represent calculated curves obtained using the corresponding external signal parameters in Eq. (2).

accumulation obtained with Sequence 2 (Fig. 3) shows that spins are sensitive to changes in all Gaussian parameters ($B_{1,max}$, t_0, σ). It is also evident that narrower Gaussian signals lead to sharper edges in the phase-accumulation curves [Figs. 3(c) and 3(g)]. This is even more evident when the amplitude of the rectangular signal is changed [Figs. 3(d) and 3(h)].

The relatively long memory time (see Sec. II C and the Supplemental Material [34]) allows us to further test signals of increased complexity using Sequence 2 (Fig. 4). To this end, we use the copper coil to generate different field shapes, in particular, a single sawtooth, the sum of a rectangular and a Gaussian signal, and two consecutive Gaussian signals. The phase accumulation changes with the different excitations sent into the coil. As expected, the general behavior for the phase accumulation is common for all signals since $\phi_{echo}(T_{seq}, s)$ changes sign when the π pulse is crossed; however, the shapes of the curves and the maximum (and minimum) amount of accumulated phase vary depending on the shape of the external signal. Additional differences can also be found in the slopes and features of the phase-accumulation curves. Moreover, the behavior of the phase accumulation calculated with Eq. (2) using the known signal parameters is in excellent agreement with experimental data (Fig. 4).

IV. DISCUSSION

A. Sensitivity

The sensitivity of the two sequences can be estimated following the definition given in Ref. [39], that is,

$$S = \frac{B_{min}}{\frac{S}{N}\sqrt{BW}}, \tag{5}$$

where B_{min} is the minimum field that can be detected, S/N is the signal-to-noise ratio, and BW is the bandwidth of the sequence. The value of B_{min} can be estimated starting from the standard deviation of the phase accumulation

TABLE I. Summary of the sensitivity S, the concentration sensitivity S_{vol}, and their lower bounds (l.b.) evaluated for Sequences 1 and 2. The values of the minimum area A_{min} are also reported for both the VO(TPP) ($\rho = 2.3 \times 10^{19}$ [15,35]) and VOPt(SOCPh)$_4$ ($\rho = 1.0 \times 10^{19}$ [38]) samples.

Sequence	S (10^{-7} T Hz$^{-\frac{1}{2}}$)		S (l.b.) (10^{-8} T Hz$^{-\frac{1}{2}}$)		S_{vol} (10^{-11} T Hz$^{-\frac{1}{2}}$ μm$^{\frac{3}{2}}$)		S_{vol} (l.b.) (10^{-12} T Hz$^{-\frac{1}{2}}$ μm$^{\frac{3}{2}}$)		A_{min} (10^{-10} T s)	
	VO(TPP)	VOPt (SOCPh)$_4$	VO(TPP)	VOPt (SOCPh)$_4$	VO(TPP)	VOPt (SOCPh)$_4$	VO(TPP)	VOPt (SOCPh)$_4$	VO(TPP)	VOPt (SOCPh)$_4$
1	2.57	–	2.87	–	5.35	–	5.98	–	1.62	1.16
2	3.98	1.54	3.12	2.72	8.30	4.89	6.51	8.63	1.61	1.10

σ_ϕ without an applied rf signal (see Supplemental Material [34]). This corresponds to the minimum phase change that can be detected under our experimental conditions. This phase value is then converted into a magnetic field using the corresponding transduction coefficient $d\phi/dB$, describing the response of the spin sensor (i.e., the phase variation per unit of applied magnetic field). The transduction coefficient is extracted from preliminary calibrations (see Supplemental Material [34]).

Using the above definitions, we find $\sigma_\phi \approx 10.4^\circ$ and $\sigma_\phi \approx 8.3^\circ$ for Sequences 1 and 2 for VO(TPP), respectively, and $\sigma_\phi \approx 4.4^\circ$ using Sequence 2 for VOPt(SOCPh)$_4$ (see Supplemental Material [34]). For VO(TPP), we obtain $B_{\mathrm{min}} = 1.14 \times 10^{-4}$ and 1.64×10^{-4} T for Sequences 1 and 2, respectively, while for VOPt(SOCPh)$_4$, the obtained value is $B_{\mathrm{min}} = 4.78 \times 10^{-5}$ T for Sequence 2. The signal-to-noise ratio is obtained by taking the amplitude of the signal at the first step of the sequence and dividing it by the noise present when the echo signal is equal to zero (see Supplemental Material [34]). The bandwidth is given by the inverse of the sequence repetition time, resulting in BW = 50 Hz (see Supplemental Material [34]). With the above values, the sensitivity obtained for VO(TPP) is $S = 2.57 \times 10^{-7}$ T Hz$^{-\frac{1}{2}}$ for Sequence 1 and $S = 3.98 \times 10^{-7}$ T Hz$^{-\frac{1}{2}}$ for Sequence 2. For VOPt(SOCPh)$_4$, the calculated sensitivity is $S = 1.54 \times 10^{-7}$ for Sequence 2.

The sensitivity values are summarized in Table I, along with their lower bounds, which are based on the Allan-variance method [40,41]. This statistical analysis, used to extract the noise floors of sensors, is implemented by calculating the grouped standard deviation of several identical repeated measurements, with B_{min} estimated from the Allan variance. The concentration sensitivity is then used to take into account the spin density (ρ) of the samples:

$$S_{\mathrm{vol}} = \frac{S}{\sqrt{\rho}}. \tag{6}$$

The resulting values are also collected in Table I.

B. Minimum detectable area (A_{min}) and memory time (T_{m})

As described by Eq. (2), the phase accumulation depends on the time integral of the signal (that is, the area A under the field strength curve). This implies that the achievable sensitivity is determined by the interplay between a given signal strength and its corresponding duration, in other words, by a minimum detectable area, A_{min}. This can be calculated for Sequences 1 and 2 from Eq. (2) using the phase noise of the echo when no external signal is applied (see Supplemental Material [34]). The obtained A_{min} values are summarized in Table I. Results are further shown in Fig. 5, where the solid curves represent the A_{min} limit for a Gaussian signal measured with VOPt(SOCPh)$_4$ using both sequences.

The upper limit for the timescale is imposed by the phase-memory time of the sample. In fact, T_{m} restricts the maximum duration of the external signal that can be measured, because the echo precession phase is lost for signals significantly longer than T_{m} (and τ). This is shown in Fig. 5 as vertical dashed and dashed-dotted lines for Sequence 1 and Sequence 2 (T_{lim}), respectively. These values are extracted from the echo phase measurement obtained during a Hahn echo sequence (see Supplemental Material [34]). Another limiting factor is the total area of the external signal, because the amplitude of the spin echo decreases as a function of the area, and this can result in a total loss of the echo signal for values that are too large (see Supplemental Material [34]). For Sequence 2, the limit for recording a full phase-accumulation curve is twice as large as that in Sequence 1. This is because τ remains fixed during the protocol. Here, we note that for signals longer than T_{lim}, it is still possible to obtain a phase-accumulation curve by using a τ shorter than the signal duration (see Supplemental Material [34]). It is worth mentioning that the resonator bandwidth can also affect the detection capability of our protocols. In fact, a cut-off value for the highest detectable Fourier component of the signal could be present, especially for signals with fast transients. Its impact can be reduced by tuning the resonator BW$_{\mathrm{r}}$ to a sufficiently large value to include most of the signal harmonics. Under our experimental conditions,

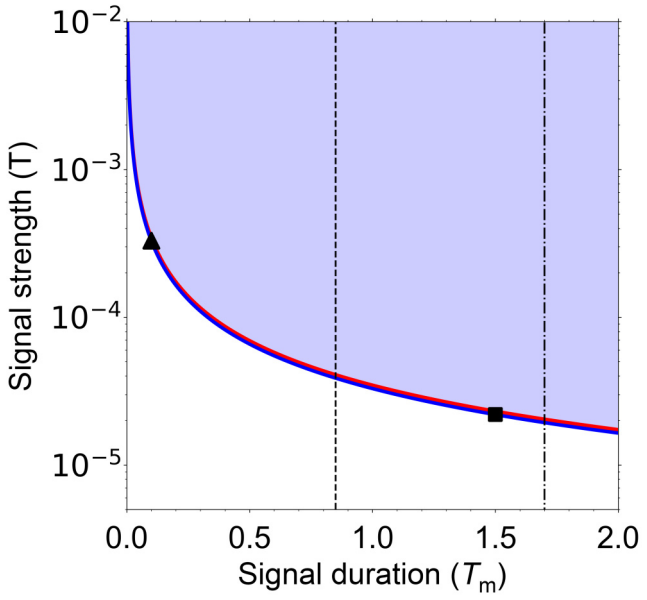

FIG. 5. Detectable areas (blue shaded) that can be measured using Sequence 1 and Sequence 2 depending on the duration of the time-domain signal and its field strength. The solid curves represent the minimum measurable area with the $VOPt(SOCPh)_4$ sample using a Gaussian signal for Sequence 1 (red line) and Sequence 2 (blue line). The signal duration is taken as 3σ [with σ being the Gaussian width in Eq. (3)]. The limit in signal duration (T_{lim}) imposed by the memory time of the sample is shown by vertical lines for Sequence 1 (dashed line) and Sequence 2 (dashed-dotted line). The markers correspond to the Gaussian signal generated by the dipolar field of an $S = 1/2$ spin located at a distance d from the sensor and undergoing a full rotation (triangle: $\sigma = 130$ ns, $d = 1.8$ nm; square: $\sigma = 1.6$ μs, $d = 4.4$ nm).

this does not significantly affect the results, as detailed in the Supplemental Material [34].

To explore some practical applications of our sensing protocols, we envisage a dimer containing a spin label (e.g., one of our quantum sensors) and a generic chemical analyte with a magnetic moment at a distance d. This dimer is diluted in a nonmagnetic matrix. Let us assume that we can induce a full spin-rotation process on the analyte from the spin value $\hbar m_s$ to $-\hbar m_s$ and back to $\hbar m_s$, giving a transient signal at the sensor site. Although more specific profiles can be considered, here we assume a Gaussian transient, solely to refer to the signal in Eq. (3), and we neglect any decrease in the memory time of our spin sensor during its rotation.

Looking at the plot in Fig. 5, a short signal of $0.1T_{\text{m}}$ duration could be detected if its field strength is at least 330 μT (triangle symbol). This corresponds to the dipolar field generated by a spin $S = 1/2$ (e.g., a radical) at $d \approx 1.8$ nm from the molecular sensor or by a spin $S = 10$ (for instance a Mn_{12} or Fe_8 single-molecule magnet) at $d \approx 3.8$ nm (always under the assumption of $g = 2$). For a long signal of $1.5T_{\text{m}}$ duration, the minimum strength of the Gaussian signal should be approximately 22 μT (square symbol). This value corresponds to the dipolar field generated by a spin $S = 1/2$ at $d \approx 4.4$ nm or by a spin $S = 10$ at $d \approx 9.4$ nm. Similarly, one may envision an application of our protocols in metal-organic-framework (MOF) architectures recently proposed to host both quantum sensors and analytes [42]. In this case, one should consider the mean field generated by a collection of analytes close to the sensor's site and collectively triggered at the same time. These values highlight that Fig. 5 may help to evaluate the feasibility of quantum sensing experiments in different realistic situations.

V. CONCLUSIONS AND OUTLOOK

We developed two quantum sensing protocols for the detection of time-dependent magnetic fields using molecular spins as detectors. These protocols expand the sensing capabilities of molecular spins beyond quantum sensing of ac magnetic fields [26]. Both our sequences have sensitivities of the order of a few $S \approx 10^{-7}$ T $\text{Hz}^{-\frac{1}{2}}$, with lower bounds approaching a few $S \approx 10^{-8}$ T $\text{Hz}^{-\frac{1}{2}}$. Although differences in experimental conditions, setups, protocols, and sensor readout techniques prevent a direct comparison, we note that sensitivity values in the 10^{-6} to 10^{-9} T $\text{Hz}^{-\frac{1}{2}}$ range have been reported for time-dependent detection and reconstruction of arbitrary signals in Ref. [29,43] for NV centers. Furthermore, we recall that sensitivity values of a few 10^{-6} T $\text{Hz}^{-\frac{1}{2}}$ have previously been reported by some of the authors of the present work, using ac magnetometry experiments based on the Hahn echo sequence with similar oxovanadyl molecular spin centers [26].

A common feature of our sequences is the minimum area of the signal that can be measured. The values are $A_{\text{min}} \approx 1.6 \times 10^{-10}$ T s for VO(TPP) and $A_{\text{min}} \approx 1.1 \times 10^{-10}$ T s for $VOPt(SOCPh)_4$. These values allow for a good trade-off between the required signal duration and the available sensitivity. In addition, Sequence 2 can be used even when the delay of the external signal with respect to the trigger is unknown. In fact, since the interpulse delay is fixed, the position shift s can be varied until $B_1(t, s)$ begins to cross the MW sequence. For these reasons, Sequence 2 is more versatile and more robust in the context of time-dependent signal detection.

As a possible future development of our protocols, we note that Sequence 2 could in principle be used to perform a full reconstruction of a time-dependent signal (see Supplemental Material [34]), similar to what was reported in Ref. [29]. This, however, requires an improvement in the signal-to-noise ratio and in the homogeneity of the MW field, achievable through optimization of the experimental setup. Another possible direction for future development relies on using machine-learning protocols, which proved

to be a successful tool for phase prediction in one of our previous works [44], to assist in the detection of the signal and, eventually, its reconstruction.

ACKNOWLEDGMENTS

The authors acknowledge the contributions of Mr. Giacomo Bellini (UniMORE), who participated in the preparation and investigation of samples, and Professor Roberta Sessoli (UniFi) for critical revision of the manuscript. This work was partially supported by the project SMILE-SQUIP funded by the Italian NQSTI National Quantum Science and Technology Institute code PE_00000023 and by the U.S. Office of Naval Research under Award No. N62909-23-1-2079. The European Research Council partially funded this work through the ERC SYNERGY project CASTLE (Grant No. 101071533).

DATA AVAILABILITY

The data that support the findings of this article are available from the authors upon reasonable request.

[1] C. L. Degen, F. Reinhard, and P. Cappellaro, Quantum sensing, Rev. Mod. Phys. **89**, 035002 (2017).
[2] N. Bar-Gill, L. Pham, A. Jarmola, D. Budker, and R. Walsworth, Solid-state electronic spin coherence time approaching one second, Nat. Commun. **4**, 1743 (2013).
[3] E. D. Herbschleb, H. Kato, Y. Maruyama, T. Danjo, T. Makino, S. Yamasaki, I. Ohki, K. Hayashi, H. Morishita, M. Fujiwara, and N. Mizuochi, Ultra-long coherence times amongst room-temperature solid-state spins, Nat. Commun. **10**, 3766 (2019).
[4] H. Zhou, J. Choi, S. Choi, R. Landig, A. M. Douglas, J. Isoya, F. Jelezko, S. Onoda, H. Sumiya, P. Cappellaro, H. S. Knowles, H. Park, and M. D. Lukin, Quantum metrology with strongly interacting spin systems, Phys. Rev. X **10**, 031003 (2020).
[5] R. Schirhagl, K. Chang, M. Loretz, and C. L. Degen, Nitrogen-vacancy centers in diamond: Nanoscale sensors for physics and biology, Annu. Rev. Phys. Chem. **65**, 83 (2014).
[6] J. M. Taylor, P. Cappellaro, L. Childress, L. Jiang, D. Budker, P. R. Hemmer, A. Yacoby, R. Walsworth, and M. D. Lukin, High-sensitivity diamond magnetometer with nanoscale resolution, Nat. Phys. **4**, 810 (2008).
[7] L. M. Pham, N. Bar-Gill, C. Belthangady, D. Le Sage, P. Cappellaro, M. D. Lukin, A. Yacoby, and R. L. Walsworth, Enhanced solid-state multispin metrology using dynamical decoupling, Phys. Rev. B **86**, 045214 (2012).
[8] L. Rondin, J.-P. Tetienne, T. Hingant, J.-F. Roch, P. Maletinsky, and V. Jacques, Magnetometry with nitrogen-vacancy defects in diamond, Rep. Prog. Phys. **77**, 056503 (2014).
[9] K. Fang, V. M. Acosta, C. Santori, Z. Huang, K. M. Itoh, H. Watanabe, S. Shikata, and R. G. Beausoleil, High-sensitivity magnetometry based on quantum beats in diamond nitrogen-vacancy centers, Phys. Rev. Lett. **110**, 130802 (2013).
[10] D. Farfurnik, A. Jarmola, D. Budker, and N. Bar-Gill, Spin ensemble-based AC magnetometry using concatenated dynamical decoupling at low temperatures, J. Opt. **20**, 024008 (2018).
[11] Z. Wang, F. Kong, P. Zhao, Z. Huang, P. Yu, Y. Wang, F. Shi, and J. Du, Picotesla magnetometry of microwave fields with diamond sensors, Sci. Adv. **8**, eabq8158 (2022).
[12] M. Atzori, E. Morra, L. Tesi, A. Albino, M. Chiesa, L. Sorace, and R. Sessoli, Quantum coherence times enhancement in vanadium(IV)-based potential molecular qubits: The key role of the vanadyl moiety, J. Am. Chem. Soc. **138**, 11234 (2016).
[13] G. A. Timco, S. Carretta, F. Troiani, F. Tuna, R. J. Pritchard, C. A. Muryn, E. J. L. McInnes, A. Ghirri, A. Candini, P. Santini, G. Amoretti, M. Affronte, and R. E. P. Winpenny, Engineering the coupling between molecular spin qubits by coordination chemistry, Nat. Nanotechnol. **4**, 173 (2009).
[14] F. Santanni and A. Privitera, Metalloporphyrins as building blocks for quantum information science, Adv. Opt. Mater. **12**, 2303036 (2024).
[15] T. Yamabayashi, M. Atzori, L. Tesi, G. Cosquer, F. Santanni, M.-E. Boulon, E. Morra, S. Benci, R. Torre, M. Chiesa, L. Sorace, R. Sessoli, and M. Yamashita, Scaling up electronic spin qubits into a three-dimensional metal organic framework, J. Am. Chem. Soc. **140**, 12090 (2018).
[16] G. Jeschke and H. Spiess, in *Novel NMR and EPR techniques*, edited by J. Dolinšek, M. Vilfan, and S. Žumer (Springer Berlin Heidelberg, Berlin, Heidelberg, 2006), p. 21.
[17] C.-J. Yu, S. von Kugelgen, D. W. Laorenza, and D. E. Freedman, A molecular approach to quantum sensing, ACS Cent. Sci. **7**, 712 (2021).
[18] E. I. Latawiec, A. Chiesa, Y. Qiu, N. A. Tcyrulnikov, R. M. Young, S. Carretta, M. D. Krzyaniak, and M. R. Wasielewski, Detecting chirality-induced spin selectivity in chromophore-linked DNA hairpins using photogenerated radical pairs, Proc. Natl. Acad. Sci. **122**, e2515120122 (2025).
[19] S. A. Dzuba, Pulsed EPR in the method of spin labels and probes, Russ. Chem. Rev. **76**, 699 (2007).
[20] F. Troiani, A. Ghirri, M. Paris, C. Bonizzoni, and M. Affronte, Towards quantum sensing with molecular spins, J. Magn. Magn. Mater. **491**, 165534 (2019).
[21] L. Sun, L. Yang, J.-H. Dou, J. Li, G. Skorupskii, M. Mardini, K. O. Tan, T. Chen, C. Sun, J. J. Oppenheim, R. G. Griffin, M. Dincă, and T. Rajh, Room-temperature quantitative quantum sensing of lithium ions with a radical-embedded metal-organic framework, J. Am. Chem. Soc. **144**, 19008 (2022).
[22] H. Singh, N. D'Souza, K. Zhong, E. Druga, J. Oshiro, B. Blankenship, R. Montis, J. A. Reimer, J. D. Breeze, and A. Ajoy, Room-temperature quantum sensing with photoexcited triplet electrons in organic crystals, Phys. Rev. Res. **7**, 013192 (2025).
[23] H. Singh, N. D'Souza, J. Garrett, A. Singh, B. Blankenship, E. Druga, R. Montis, L. Z. Tan, and A. Ajoy, High sensitivity pressure and temperature quantum sensing in pentacene-doped p-terphenyl single crystals, Nat. Commun. **16**, 10530 (2025).

[24] A. Privitera, A. Chiesa, F. Santanni, A. Carella, D. Ranieri, A. Caneschi, M. D. Krzyaniak, R. M. Young, M. R. Wasielewski, S. Carretta, and R. Sessoli, Room-temperature optical spin polarization of an electron spin qudit in a vanadyl-free base porphyrin dimer, J. Am. Chem. Soc. **147**, 331 (2025).

[25] N. Grzegorzek, H. Mao, P. Michel, M. J. Junge, E. R. Lorenzo, R. M. Young, M. D. Krzyaniak, M. R. Wasielewski, and E. T. Chernick, Metalated porphyrin stable free radicals: exploration of electron spin communication and dynamics, J. Phys. Chem. A **124**, 6168 (2020).

[26] C. Bonizzoni, A. Ghirri, F. Santanni, and M. Affronte, Quantum sensing of magnetic fields with molecular spins, Npj Quantum Inf. **10**, 1 (2024).

[27] C. Bonizzoni, A. Ghirri, F. Santanni, M. Atzori, L. Sorace, R. Sessoli, and M. Affronte, Storage and retrieval of microwave pulses with molecular spin ensembles, Npj Quantum Inf. **6**, 68 (2020).

[28] A. Cooper, E. Magesan, H. N. Yum, and P. Cappellaro, Time-resolved magnetic sensing with electronic spins in diamond, Nat. Commun. **5**, 3141 (2014).

[29] J. Zopes and C. L. Degen, Reconstruction-free quantum sensing of arbitrary waveforms, Phys. Rev. Appl. **12**, 054028 (2019).

[30] A. Cooper, E. Magesan, H. N. Yum, and P. Cappellaro, Time-resolved magnetic sensing with electronic spins in diamond, Nat. Commun. **5**, 3141 (2014).

[31] E. Magesan, A. Cooper, H. Yum, and P. Cappellaro, Reconstructing the profile of time-varying magnetic fields with quantum sensors, Phys. Rev. A **88**, 032107 (2013).

[32] J. R. Maze, P. L. Stanwix, J. S. Hodges, S. Hong, J. M. Taylor, P. Cappellaro, L. Jiang, M. V. G. Dutt, E. Togan, A. S. Zibrov, A. Yacoby, R. L. Walsworth, and M. D. Lukin, Nanoscale magnetic sensing with an individual electronic spin in diamond, Nature **455**, 644 (2008).

[33] E. L. Hahn, Spin echoes, Phys. Rev. **80**, 580 (1950).

[34] See Supplemental Material at http://link.aps.org/supplemental/10.1103/56hv-qp5d for further details.

[35] M. G. Drew, P. C. Mitchell, and C. E. Scott, Crystal and molecular structure of three oxovanadium(IV) porphyrins: Oxovanadium tetraphenylporphyrin(I), oxovanadium(IV) etioporphyrin(II) and the 1:2 adduct of (II) with 1,4-dihydroxybenzene(III). Hydrogen bonding involving the VO group. Relevance to catalytic demetallisation, Inorganica Chim. Acta **82**, 63 (1984).

[36] S. A. Beach, J. L. Guillet, S. P. Lagueux, M. Perfetti, B. N. Livesay, M. P. Shores, J. W. Bacon, A. L. Rheingold, P. L. Arnold, and L. H. Doerrer, Heterotrimetallic {LnOVPt} complexes with antiferromagnetic Ln–V coupling and magnetic memory, Chem. Commun. **56**, 11062 (2020).

[37] M. Imperato, A. Nicolini, M. Borsari, M. Briganti, M. Chiesa, Y.-K. Liao, A. Ranieri, A. Raza, E. Salvadori, L. Sorace, and A. Cornia, Quantum spin coherence and electron spin distribution channels in vanadyl-containing lantern complexes, Inorg. Chem. Front. **11**, 186 (2024).

[38] G. Bellini, *Synthesis and properties of molecular qubits based on heterobimetallic paddlewheel complexes*, Master's thesis, University of Modena and Reggio Emilia (2025), available at https://morethesis.unimore.it/theses/available/etd-03192025-184558/.

[39] A. Blank, Y. Twig, and Y. Ishay, Recent trends in high spin sensitivity magnetic resonance, J. Magn. Reson. **280**, 20 (2017).

[40] K. Draganová, F. Kmec, J. Blazek, D. Praslička, J. Hudák, and M. Laššák, Noise analysis of magnetic sensors using Allan variance, Acta Phys. Pol., A **126**, 394 (2014).

[41] M. B. Marinov, B. Ganev, N. Djermanova, and T. D. Tashev, in *2019 IEEE XXVIII International Scientific Conference Electronics (ET)* (IEEE, Sozopol, Bulgaria, 2019), p. 1.

[42] L. Sun, L. Yang, J.-H. Dou, J. Li, G. Skorupskii, M. Mardini, K. O. Tan, T. Chen, C. Sun, J. J. Oppenheim, R. G. Griffin, M. Dincă, and T. Rajh, Room-temperature quantitative quantum sensing of lithium ions with a radical-embedded metal–organic framework, J. Am. Chem. Soc. **144**, 19008 (2022).

[43] G. Balasubramanian, P. Neumann, D. Twitchen, M. Markham, R. Kolesov, N. Mizuochi, J. Isoya, J. Achard, J. Beck, J. Tissler, V. Jacques, P. R. Hemmer, F. Jelezko, and J. Wrachtrup, Ultralong spin coherence time in isotopically engineered diamond, Nat. Mater. **8**, 383 (2009).

[44] C. Bonizzoni, M. Tincani, F. Santanni, and M. Affronte, Machine-learning-assisted manipulation and readout of molecular spin qubits, Phys. Rev. Appl. **18**, 064074 (2022).